

# UCLA

## UCLA Previously Published Works

### Title

Ultrafast optical melting of trimer superstructure in layered 1T'-TaTe2

### Permalink

<https://escholarship.org/uc/item/5zh399bc>

### Journal

Communications Physics, 4(1)

### ISSN

2399-3650

### Authors

Siddiqui, Khalid M

Durham, Daniel B

Cropp, Frederick

et al.

### Publication Date

2021

### DOI

10.1038/s42005-021-00650-z

Peer reviewed

## Ultrafast optical melting of trimer superstructure in layered 1T'-TaTe<sub>2</sub>

Khalid M. Siddiqui<sup>1,9</sup>, Daniel B. Durham<sup>2,3,9</sup>, Frederick Cropp<sup>4,5</sup>, Colin Ophus<sup>2,6</sup>, Sangeeta Rajpurohit<sup>6</sup>, Yanglin Zhu<sup>7</sup>, Johan D. Carlström<sup>6</sup>, Camille Stavrakas<sup>6</sup>, Zhiqiang Mao<sup>7</sup>, Archana Raja<sup>6</sup>, Pietro Musumeci<sup>4</sup>, Liang Z. Tan<sup>6</sup>, Andrew M. Minor<sup>2,3</sup>, Daniele Filippetto<sup>5</sup>✉ & Robert A. Kaindl<sup>1,8</sup>✉

Quasi-two-dimensional transition-metal dichalcogenides are a key platform for exploring emergent nanoscale phenomena arising from complex interactions. Access to the underlying degrees-of-freedom on their natural time scales motivates the use of advanced ultrafast probes sensitive to self-organised atomic-scale patterns. Here, we report the ultrafast investigation of TaTe<sub>2</sub>, which exhibits unique charge and lattice trimer order characterised by a transition upon cooling from stripe-like chains into a (3 × 3) superstructure of trimer clusters. Utilising MeV-scale ultrafast electron diffraction, we capture the photo-induced TaTe<sub>2</sub> structural dynamics – exposing a rapid  $\approx 1.4$  ps melting of its low-temperature ordered state followed by recovery via thermalisation into a hot cluster superstructure. Density-functional calculations indicate that the initial quench is triggered by intra-trimer Ta charge transfer which destabilises the clusters, unlike melting of charge density waves in other TaX<sub>2</sub> compounds. Our work paves the way for further exploration and ultimately rapid optical and electronic manipulation of trimer superstructures.

<sup>1</sup>Materials Sciences Division, Lawrence Berkeley National Laboratory, Berkeley, CA, USA. <sup>2</sup>National Center for Electron Microscopy, Molecular Foundry, Lawrence Berkeley National Laboratory, Berkeley, CA, USA. <sup>3</sup>Department of Materials Science and Engineering, University of California at Berkeley, Berkeley, CA, USA. <sup>4</sup>Department of Physics and Astronomy, University of California Los Angeles, Los Angeles, CA, USA. <sup>5</sup>Accelerator Technology and Applied Physics Division, Lawrence Berkeley National Laboratory, Berkeley, CA, USA. <sup>6</sup>Molecular Foundry, Lawrence Berkeley National Laboratory, Berkeley, CA, USA. <sup>7</sup>Department of Physics, The Pennsylvania State University, University Park, PA, USA. <sup>8</sup>Department of Physics, Arizona State University, Tempe, AZ, USA. <sup>9</sup>These authors contributed equally: Khalid M. Siddiqui, Daniel B. Durham. ✉email: [dfilippetto@lbl.gov](mailto:dfilippetto@lbl.gov); [kaindl@asu.edu](mailto:kaindl@asu.edu)

**H**arnessing emergent orders in quantum materials has the potential to revolutionise energy and information technologies<sup>1</sup>. Complex interactions between lattice, electron, and spin degrees-of-freedom in these systems can give rise to emergent physics, such as unconventional superconductivity<sup>2</sup>, topological protection<sup>3,4</sup>, or charge density wave (CDW) order and tailored interactions in two-dimensional (2D) materials<sup>5</sup>. Traditionally, control of materials has been achieved by adiabatic tuning of external parameters. Alternatively, ultrashort light pulses can be employed to perturb and transform states in quantum materials on femtosecond timescales<sup>6,7</sup>. The quest to probe and control electronic and lattice structural dynamics in solids has driven the utilisation of advanced ultrafast spectroscopies, including ultrafast X-ray and electron diffraction<sup>8–13</sup>, multi-terahertz fields<sup>14–16</sup>, and time-resolved photoemission<sup>17–19</sup>.

Tantalum dichalcogenides ( $\text{TaX}_2$ ,  $\text{X} = \text{S}, \text{Se}, \text{Te}$ ) represent a class of materials that are well-matched for this pursuit, and have gained increasing attention as quasi-2D systems with enhanced Coulomb and electron–lattice interactions<sup>20–22</sup>. These compounds exhibit rich phase diagrams, including semi-metallic, charge-ordered, and superconducting behaviours. Multiple CDW phases are observed in  $1\text{T-TaS}_2$ , which has spawned numerous ultrafast studies to clarify the formation mechanisms and phase competition<sup>23–25</sup>. Moreover, ultrafast driving exposed novel metastable phases in these systems, resulting in a new paradigm of hidden states<sup>26,27</sup>. Members of the  $1\text{T-TaSe}_{2-x}\text{Te}_x$  family exhibit varying polytypes, CDW ground states, as well as superconductivity depending on composition<sup>28</sup>. Ultrafast optical melting and switching between CDW phases have so far been demonstrated in  $\text{TaSe}_2$  and in  $\text{TaSe}_{2-x}\text{Te}_x$  alloys, accessing a range of dynamical pathways and timescales<sup>29–31</sup>.

Curiously eluding ultrafast investigation thus far is  $\text{TaTe}_2$ . This compound exhibits markedly different properties with respect to the other Ta dichalcogenides, attributed to weaker electronegativity of Te with respect to Ta leading to a strong propensity for charge transfer and metal–metal bonding<sup>32–34</sup>.  $\text{TaTe}_2$  exhibits stronger electron–phonon coupling, higher charge-order binding energy, and larger lattice distortions than  $\text{TaS}_2$  and  $\text{TaSe}_2$  compounds<sup>22,35</sup>. The room temperature distorted monoclinic  $1\text{T}'$  crystal structure is characterised by an intra-layer  $(3 \times 1)$  linear stripe-like order composed of double zigzag Ta trimer chains. A structural transition into a phase with  $(3 \times 3)$  order occurs at  $T_{\text{PT}} = 174 \text{ K}$ , with Ta atoms forming trimer clusters along the linear chains with commensurate CDW-like order<sup>33,36–38</sup>. Unlike other  $\text{TaX}_2$  CDW systems<sup>39,40</sup>, the low-temperature (LT) phase ordering of  $\text{TaTe}_2$  exhibits metallic behaviour, with enhanced conductivity and magnetic susceptibility<sup>41</sup>. However, the ultrafast response of this compound to optical driving remains unknown. This motivates the use of advanced structural probes to follow the evolution of distortions and periodic order, as a measure of underlying interactions.

We report the ultrafast investigation of  $\text{TaTe}_2$ , demonstrating a rapid picosecond melting of its trimer cluster lattice superstructure in the LT phase. Ultrafast electron diffraction (UED) with relativistic electron bunches is applied using the High Repetition-rate Electron Scattering (HiRES) beamline<sup>42–44</sup> to probe the time evolution of lattice order after intense near-infrared (near-IR) excitation. We observe photo-induced melting of the LT order on a  $\approx 1.4 \text{ ps}$  timescale, indicative of fast switching, followed by recovery into a hot  $(3 \times 3)$  trimer phase. Insight into the nature of trimer cluster melting is obtained via density functional calculations, which indicate an initial quench driven by charge-transfer transitions from bonding to non-bonding states of the Ta trimer—suggesting pathways for a photo-induced transition that is unique among the family of  $\text{TaX}_2$  materials. This

work establishes  $\text{TaTe}_2$  as a promising material for optical control, motivating examination of concomitant electronic dynamics for device applications.

## Results

### Crystal structure and signatures of structural phase transition.

Figure 1a illustrates the crystal structure of  $\text{TaTe}_2$  in its LT phase. Triple-layer sheets of covalently bonded Ta and Te atoms are separated by weaker van der Waals forces along the stacking direction. Prominent structural elements in this material are Ta trimers—sets of three adjacent Ta atoms in a row that cluster together via enhanced Ta–Ta bonding. Already at room temperature, Ta atoms are ordered in-plane into trimers assembled into double zigzag chains along the  $b$ -axis, which breaks hexagonal symmetry and forms a three-layer stacking sequence. In the LT phase, additional ordering emerges in the chains along the  $b$ -axis in the form of trimer clusters. This  $(3 \times 3)$  lattice superstructure represents a distorted  $1\text{T}'$  polytype with  $C2/m$  space group symmetry and a monoclinic unit cell<sup>45</sup>. In this configuration, each Ta atom in the unit cell is coordinated to six Te atoms in a periodically distorted octahedral arrangement.

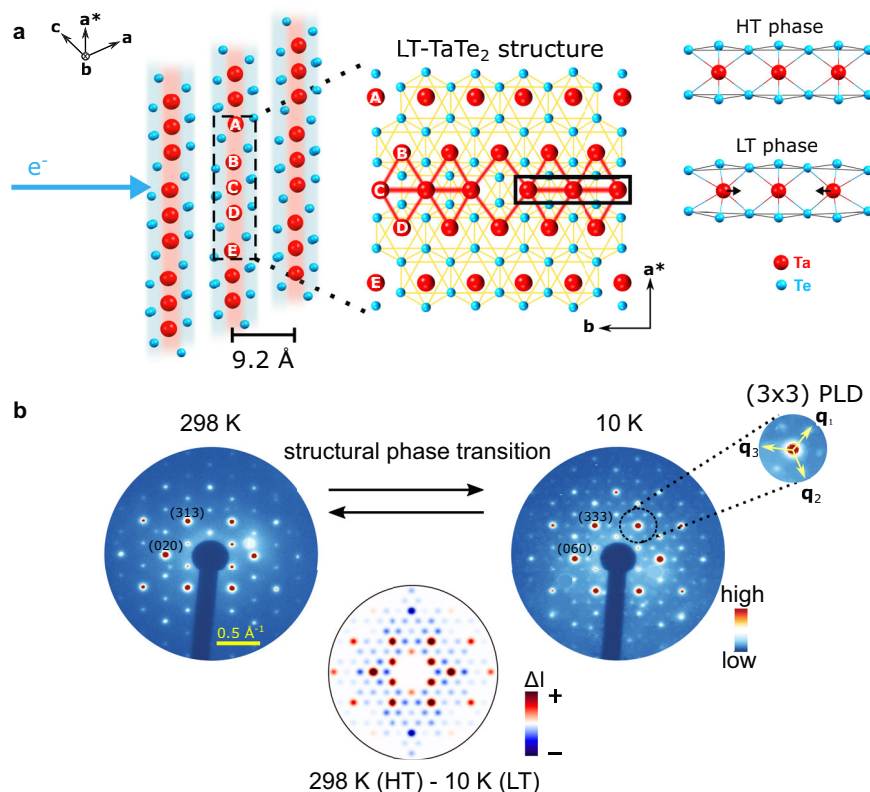
Our density functional theory (DFT) calculations of relaxed structures of  $\text{TaTe}_2$  confirm the distortions due to an atomic ordering of Ta atoms attributed to metal–metal bonding, in agreement with the structures previously determined by X-ray diffraction<sup>33</sup>. Moreover, our calculations also reveal enhanced Ta–Ta bonds along the  $b$ -axis in the LT phase as highlighted in Fig. 1a, resulting in the tripling along the  $b$ -axis corresponding to an overall  $(3 \times 3)$  superstructure (cf. Supplementary Note 1 for additional details).

Figure 1b shows equilibrium diffraction patterns of a  $1\text{T}'$ - $\text{TaTe}_2$  flake which we measured with the 0.75 MeV electron bunches at HiRES, comparing the high-temperature (HT) phase at 298 K and LT phase at 10 K. As illustrated in Fig. 1a, the electron beam impinges along the  $[101]$  zone axis, i.e., perpendicular to the Ta and Te layers. The measured diffraction patterns exhibit a large number of Bragg spots reaching up to high momentum transfer, demonstrating both a high sample crystallinity and a large scattering range afforded by the relativistic beam energy. More details about the sample and its preparation, including transport measurements, are given in the “Methods” and in Supplementary Note 2.

At 298 K, we observe twofold symmetry exemplified, for instance, by differences of the (020) and (313) Bragg peaks in intensity and their relative distance from the centre. This is consistent with the  $(3 \times 1)$  periodicity and the monoclinic crystal structure.

The pattern at 10 K in Fig. 1b reveals the appearance of new satellite peaks surrounding the main lattice peaks as a result of the emergent  $(3 \times 3)$  periodic lattice distortion (PLD), in concordance with Ta trimer cluster formation and the associated unit cell tripling<sup>33,36–38</sup>. Their observation also demonstrates that the transverse coherence length of the electron source is sufficient to track the dynamics of the LT superstructure in  $1\text{T}'$ - $\text{TaTe}_2$ . Analogous satellite peaks in the HT phase are  $\approx 1000$  times weaker than the main Bragg peaks and are not observed in these measurements (see Supplementary Note 2).

To determine the signature in the electron diffraction patterns attributed to the structural phase transition, we calculate the difference between HT and LT patterns, following normalisation by the total electron intensity. The resulting changes are shown at the bottom of Fig. 1b. While all superlattice satellites associated with the  $(3 \times 3)$  trimer superstructure are suppressed, the main Bragg peaks exhibit a mixture of positive and negative intensity changes. This complex response deviates from observations in



**Fig. 1 Crystal structure and electron diffraction patterns at thermal equilibria.** **a** Layered crystal structure of the low-temperature phase of 1T'-TaTe<sub>2</sub>. The electron beam is incident perpendicular to Ta and Te planes in the ultrafast electron diffraction (UED) experiments. The *a*, *b*, and *c* lattice vectors shown are those of the monoclinic unit cell. The projection perpendicular to the dashed region is indicated. Black box: Ta trimer clusters forming along the *b*-axis in the low-temperature (LT) phase. Representations of LT and high-temperature (HT) phases showing enhanced distortions in the LT phase are presented in the top right. Small black arrows denote the movement of atoms towards the central Ta atom. **b** Static electron diffraction patterns of 1T'-TaTe<sub>2</sub> obtained by 0.75 MeV electron pulses at 298 K (HT) and 10 K (LT) along the [101] zone axis. Note the different indices for the LT pattern due to tripling along the *b*-axis. The inset shows the (3 × 3) periodic lattice distortion satellite (superlattice) peaks that arise in the LT phase. A few additional peaks are present due to diffraction from the Si support frame (see Supplementary Note 2 for sample details). The symmetrised difference pattern between HT and LT phases is shown below the static patterns, with contributions from the Si frame and silicon nitride (Si<sub>3</sub>N<sub>4</sub>) membrane removed. The colour scale gives the absolute diffracted intensity change ( $\Delta I$ ).

TaSe<sub>2</sub> and TaS<sub>2</sub>, where all primary Bragg peaks increased in intensity, opposite to the suppression of the PLD satellites<sup>23,46</sup>. We attribute this positive–negative intensity change signature to the symmetry of the superstructure formation within the distorted monoclinic unit cell, leading to mixed structure factor changes for different diffraction orders as supported by our simulations (see Supplementary Note 3)<sup>47,48</sup>.

**Ultrafast optical melting of trimer clusters.** We utilise the HiRES beamline for UED. The sample was first cooled into the LT ordered phase at 10 K, and then photo-excited with near-IR femtosecond pulses (1030 nm wavelength). Time-delayed electron pulses at 0.75 MeV are used as structural probe, as illustrated in Fig. 2a. Recorded diffraction patterns with and without excitation provide signatures of photo-induced changes for each pump-probe time delay.

Difference maps of the diffraction intensity at selected time delays  $\Delta t$  are shown in Fig. 2b for a pump fluence of 2.3 mJ cm<sup>-2</sup>, indicating structural changes on a picosecond timescale. For clearer visualisation, these maps are symmetrised by averaging signals across the vertical and horizontal mirror plane symmetries (the process is described in Supplementary Note 4). At early times, the signals exhibit a characteristic pattern of changes, including a decrease of the (3 × 3) PLD satellites, and a mixture of increased and decreased intensities of the main lattice Bragg

peaks (see diffraction pattern at  $\Delta t = 4$  ps in Fig. 2b). This pattern strongly resembles that of the HT–LT phase transition obtained from the equilibrium data in Fig. 1a. This indicates that the intense near-IR excitation induces a melting of the LT trimer clusters and an ultrafast phase transition to the (3 × 1) ordered HT state in TaTe<sub>2</sub>.

In order to track the structural kinetics, we fit all peaks for each time-delayed UED pattern, summing the photo-induced changes of specific subsets for optimal signal-to-noise (the peak fitting procedure is provided in Supplementary Note 5). Figure 2c plots the dynamics of the set of lattice Bragg peaks exhibiting an intensity increase (Bragg $\uparrow$ ) or decrease (Bragg $\downarrow$ ) in the pattern, as well as the changes of the superlattice satellites. Normalised to their intensities before excitation, the PLD satellites undergo  $\approx 55\%$  suppression with a time constant of  $\tau_{\text{PLD}} \approx 1.4$  ps (details of the fitting are provided in Supplementary Note 6). This time constant provides a measure of the (3 × 3) trimer superstructure melting time in TaTe<sub>2</sub> in our experiments. We note this is likely preceded by a faster electronic melting time, which we cannot access here, but could be a subject of future spectroscopic investigations<sup>17</sup>.

Alongside the PLD suppression, the primary lattice Bragg peaks also exhibit strong changes with slower dynamics corresponding to time constants of  $\tau_{\text{Bragg}\uparrow} \approx 2.4$  ps and  $\tau_{\text{Bragg}\downarrow} \approx 2.3$  ps. The underlying diffraction orders show comparable

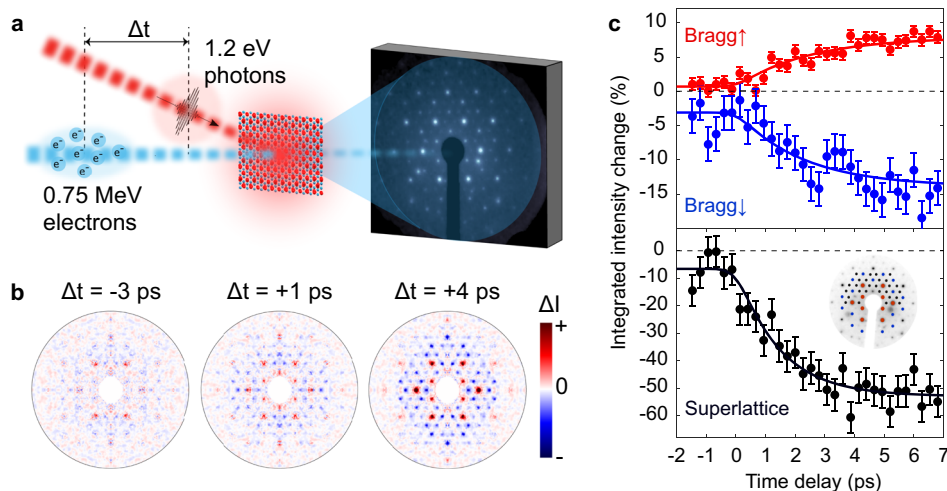


**Fig. 2 Ultrafast electron diffraction of TaTe<sub>2</sub>.** **a** Illustration of the optical pump, electron diffraction probe experiment. **b** Photo-induced changes in the diffraction patterns, for selected time delays. The colour scale gives the absolute diffracted intensity change ( $\Delta I$ ). The patterns have been symmetrised for visualisation purposes only. **c** Temporal evolution of the signals from the main lattice Bragg peaks, separately for the increasing and decreasing subsets, and of the low-temperature (LT) phase superlattice peaks. Solid lines: fits with an exponential function convolved with the time resolution of 0.75 ps, up to 7 ps delay time. The corresponding time constants are  $\tau_{\text{PLD}} = 1.44 \pm 0.27$  ps for the superlattice peaks and  $\tau_{\text{Bragg}\uparrow} = 2.44 \pm 0.81$  ps and  $\tau_{\text{Bragg}\downarrow} = 2.25 \pm 1.34$  ps for the main lattice peak subsets. Error bars in the data indicate standard error calculated using the distribution of laser-off signals compared to the mean laser-off signal over the course of the measurement.

dynamics (see Supplementary Note 7). Moreover, an oscillation seems to appear in the Bragg↓ trace, with a period of  $\approx 2$  ps. While this may be linked to excitation of coherent phonons, the  $\approx 0.5$  THz frequency does not match vibrational modes identified by theory (cf. Supplementary Note 1). The lack of a similar feature on the Bragg↑ curve does not rule out a coherent phonon origin. However, the error bars in the Bragg↓ trace are larger due to its weaker constituent high- $q$  peaks (cf. Supplementary Note 7) and the fluctuation is comparable to measurement error. While beyond the scope of our present work, future investigations are warranted to clarify the presence of coherent lattice motion. We also note that at negative time delays, a few-percent intensity reduction is observed in both the superlattice and Bragg↓ peaks, which we attribute to residual heating accumulated over several laser pulses.

**Re-formation of lattice superstructure.** Following the melting of the trimer clusters, further structural dynamics ensues that is marked by the recovery of the  $(3 \times 3)$  superstructure due to lattice thermalisation. Figure 3a shows transient difference maps, where the data have been averaged for two representative time ranges corresponding to early ( $\Delta t = 3\text{--}5$  ps) and late (50–80 ps) time delays. The pattern at early times exhibits the clear signature of the  $(3 \times 3)$  trimer superstructure melting discussed above, while at later times such signature disappears and the pattern recovers the LT superlattice. The broad overall reduction of the peak intensities in this time range is that expected of a heated state with incoherent thermal atomic motions via the Debye–Waller effect<sup>46,49</sup>. Between these time ranges, we note that diffraction peaks on one side of the pattern increase while those on the other side decrease, indicating mechanical buckling of the sample as it accommodates the structural phase change and lattice heating<sup>50,51</sup>. Difference images from these time ranges are shown in Supplementary Note 4.

As seen in Fig. 3b—which plots the time evolution of the PLD side peaks over the entire measurement window—the suppressed trimer order recovers  $\approx 20\%$  of the original intensity with a  $\approx 7$  ps time constant. We note that this timescale may be influenced by simultaneous contribution from mechanical buckling. The overall

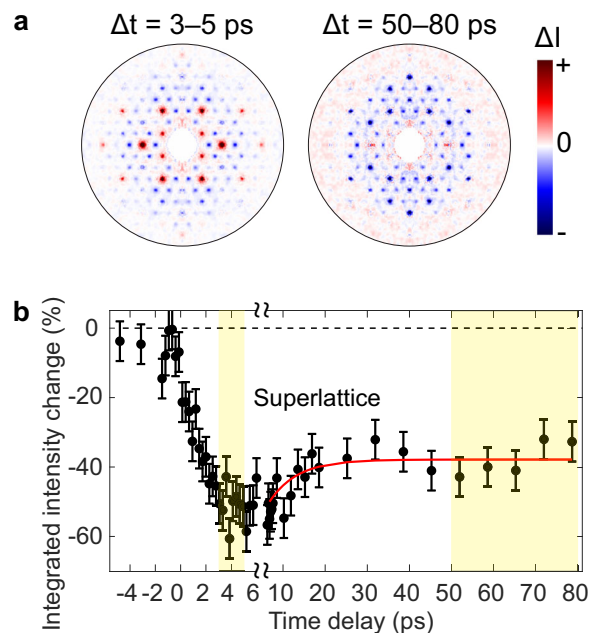


**Fig. 3 Re-formation of superstructure and Debye–Waller dynamics.**

**a** Representative symmetrised difference images for early (centred around  $\approx 4$  ps) and late (around  $\approx 65$  ps) time delays. The colour scale gives the absolute diffracted intensity change ( $\Delta I$ ). For improved signal-to-noise these are calculated by averaging difference patterns over time ranges, i.e., 3–5 ps for early and 50–80 ps for late time delays. For the late time delays, all Bragg peaks exhibit a loss of intensity indicative of a Debye–Waller effect. **b** Dynamics of the superlattice peaks over an extended timescale. Yellow shading indicates time ranges that were averaged to generate the difference images. A partial recovery is observed, fit with an exponential relaxation with offset (red line) with time constant  $\tau = 6.6 \pm 2.6$  ps. The long-lived suppression indicates that the lattice system has thermalised at an elevated temperature. Error bars in the data indicate standard error calculated using the distribution of laser-off signals compared to the mean laser-off signal over the course of the measurement.

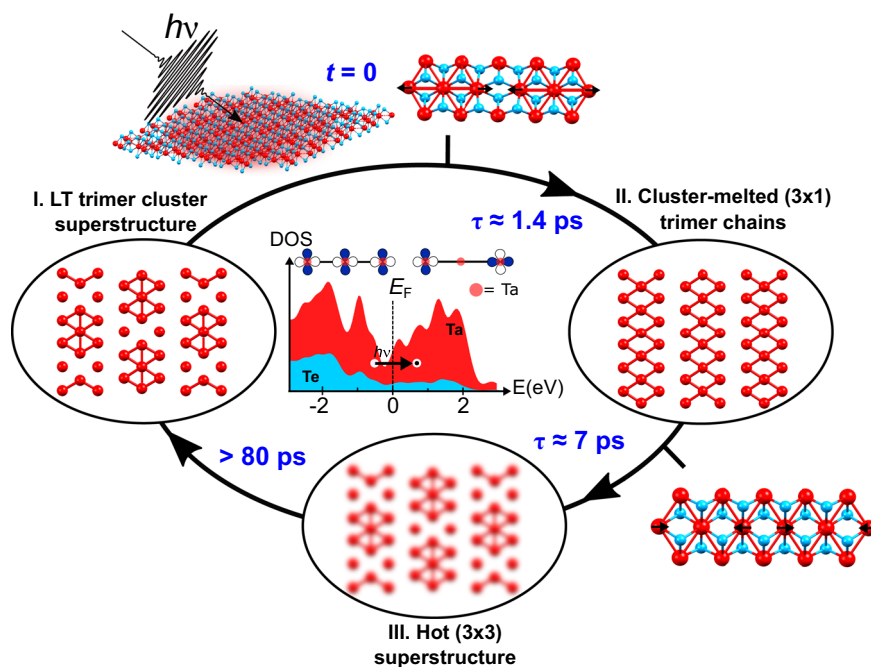


**Fig. 4 Proposed stages of the photo-induced dynamics in 1T'-TaTe<sub>2</sub>.** The system starts in the low-temperature (LT) phase with a (3 × 3) superstructure of Ta trimer clusters (I). Near-infrared excitation promotes carriers from bonding to non-bonding states via a charge-transfer excitation, which results in melting of the trimer clusters and leaves behind stripe-like trimer chains (II). Subsequently, the lattice subsystem thermalises, causing the (3 × 3) superstructure to re-establish and stabilise at elevated temperatures (III). Inset: density of states (DOS) projected onto Ta and Te atoms as calculated using density functional theory, along with schematic optically induced promotion from bonding to non-bonding Ta orbitals, which lie in the plane.  $E_F$  denotes the Fermi level. The participating Ta trimer bonding and non-bonding (with a node in the middle) orbitals are shown.

suppression of the diffraction peaks relative to the LT ground state indicates the thermalisation of the lattice degrees-of-freedom into a “hot” (3 × 3) trimer superstructure at longer delays. We can estimate the maximum lattice thermalised temperature due to full thermalisation of the absorbed laser energy. For the given  $2.3 \text{ mJ cm}^{-2}$  fluence, this results in a temperature of 177 K, based on the 1T'-TaTe<sub>2</sub> heat capacity<sup>33</sup> and the optical constants we measured of our 60-nm thick flake (see Supplementary Notes 8 and 9). We also performed experiments on the same sample at 1.75 and  $1.5 \text{ mJ cm}^{-2}$  fluence. The signature of the structural phase transition was reproduced for these fluences with reduced magnitude (see Supplementary Note 9).

## Discussion

Figure 4 illustrates the proposed sequence of phases in the ultrafast dynamics of TaTe<sub>2</sub>. Photo-excitation with intense pulses leads to the excitation of energetic carriers and picosecond melting of the LT (3 × 3) trimer superstructure phase. The transient phase that results corresponds to a (3 × 1) trimer chain order, as inferred from the close overlap of the photo-induced change in the diffraction pattern with the fingerprint of the LT–HT transition. In the subsequent picoseconds, the lattice degrees-of-freedom thermalise, enhancing Ta–Ta bonds and thereby switching into a hot (3 × 3) superstructure state. The latter persists for extended times ( $\gg 80 \text{ ps}$ ) until thermal diffusion transfers heat into the substrate.

DFT calculations clarified the electronic states involved in the photo-excitation. We computed the projected density of states and crystal orbital Hamilton population (COHP) of the relaxed LT and HT structures of TaTe<sub>2</sub>, revealing the nature of occupied and unoccupied states, as shown in Fig. 4 (see Supplementary Note 1 for details and Supplementary Data 1 for atomic coordinates of the calculated relaxed structures). In the LT phase, the

lower-energy region of the valence band (i.e., below  $-4 \text{ eV}$ ) consists of Te *p*-states with a small contribution from Ta *d*-states, whereas the upper region of the band (i.e., above  $-2 \text{ eV}$ ) has mostly Ta character. Negative COHP values in the upper valence band indicate the bonding nature of Ta trimer states in this energy region. Trimer formation is enabled by partial charge transfer from Te to Ta involving  $d_{xz}$  and  $d_{xy}$  states, which leaves uneven charges on Ta sites and enhanced Ta–Ta bonding<sup>36</sup>. Meanwhile, conduction band states near the Fermi level belong to non-bonding states of Ta trimers, with anti-bonding states lying higher in energy ( $\approx 4 \text{ eV}$  above  $E_F$ ).

Optical absorption in 1T'-TaTe<sub>2</sub> involves mainly two kinds of dipole-allowed charge-transfer transitions (see Supplementary Note 1): promoting either Te *p* to Ta anti-bonding states (type-I), or depopulating bonding states while populating non-bonding states of the *b*-axis trimers above the Fermi level (type-II). Photo-excitation around  $1.2 \text{ eV}$  chiefly involves the latter, which weakens the original charge disproportionation between Ta sites within these trimers, thus triggering the “melting” of the (3 × 3) order. The calculations also identified several strongly coupled phonons, including a mode around  $2.7 \text{ THz}$  involving Te motions and displacements of the Ta ions along the trimer axes that may be set into motion after optical charge-transfer excitation. This predicts a cooperative mechanism for photo-induced trimer cluster dissolution in TaTe<sub>2</sub>, which can be addressed in future diffraction studies with higher temporal resolution and time-resolved diffuse scattering to directly track the phonon modes participating in the transformation.

Our study hence represents the first ultrafast measurement of TaTe<sub>2</sub>, utilising short MeV electron bunches to resolve a picosecond atomic-scale melting of its intriguing trimer clusters and the subsequent thermalisation into a hot (3 × 3) superstructure phase. In these and other MTe<sub>2</sub> systems (where M = transition metal), changes in the lattice structure are linked to anomalous

changes in conductivity and magnetic susceptibility. The light-driven toggle and recovery seen here to occur between different lattice symmetries may thus enable applications, e.g., for ultrafast switching. Moreover, the associated trimer dynamics in this material opens the possibility for control of the related electronic modulations in TaTe<sub>2</sub> on even faster timescales.

## Methods

**Ultrafast electron diffraction.** The UED experiments were performed at the HiRES beamline at Lawrence Berkeley National Laboratory (LBNL). The instrument exploits a one-of-a-kind technology developed at LBNL to provide unique beam properties for ultrafast structural dynamics studies, coupling relativistic electrons and high repetition rates. The results reported in the paper validate the technological breakthrough, which has the potential of broadening the scientific reach of ultrafast tools. Near-IR laser pulses centred at  $\approx 1030$  nm wavelength and with  $\approx 350$  fs duration (full-width at half-maximum, FWHM) were used to photo-excite the sample. Synchronised electron pulses with 0.75 MeV kinetic energy (de Broglie wavelength  $\lambda = 0.01$  Å) were delivered to the sample for electron diffraction. Experiments were performed at 0.5 kHz repetition rate, recording ten frames with the pump beam OFF and ten frames with the pump ON for each time delay. Each frame was recorded for an exposure time of 8 s. A home-built sample stage interfaced to a closed-cycle cryostat was used to cryogenically cool the samples down to 10 K. Laser and electron beams impinged on the TaTe<sub>2</sub> sample surface, transmitting through a supporting silicon nitride window. The electron beam diameter at the sample was  $\approx 450$   $\mu$ m FWHM, while the pump beam was adjusted to  $\approx 750$   $\mu$ m FWHM to ensure homogeneous excitation across the probe volume. The beam charge was  $\approx 2.5$  fC corresponding to  $1.6 \times 10^4$  electrons/pulse. We confirmed sample reversibility by measuring intensities of the diffraction peaks in pump OFF images normalised to their intensities before excitation as a function of pump laser shots (see Supplementary Note 10).

**TaTe<sub>2</sub> samples.** Single crystals of 1T'-TaTe<sub>2</sub> were grown by the chemical vapour transport technique<sup>59</sup> at 700–800 °C for 14 days using iodine as a transport agent. The crystals were repeatedly mechanically exfoliated with Scotch tape until optically transparent and then dry transferred onto 20-nm thick Si<sub>3</sub>N<sub>4</sub> windows using polydimethylsiloxane stamps<sup>53</sup>. The thickness of the TaTe<sub>2</sub> flake was determined to be  $\approx 60$  nm using atomic force microscopy (AFM; see Supplementary Note 2).

**Simulations, image analysis, and standard error.** Details of DFT calculations, electron diffraction simulations, and diffraction image analysis methods are provided in Supplementary Notes 1, 3, and 4, respectively. The Supplementary Data 1 file contains the atomic coordinates of the relaxed structures. The error bars in Figs. 2c and 3b represent the standard error for the given number of averaged frames. The corresponding standard deviation per frame is derived (for each peak set Bragg $\uparrow$ , Bragg $\downarrow$ , and superlattice) from the distribution of laser-off frames, multiplied by  $\sqrt{2}$  to account for the total standard deviation when subtracting (laser on) – (laser off) frames.

## Data availability

The data that support the findings of this study are available from the corresponding authors upon reasonable request.

## Code availability

The codes that support the findings of this study are available from the corresponding authors upon reasonable request.

Received: 9 October 2020; Accepted: 8 June 2021;

Published online: 02 July 2021

## References

- Tokura, Y., Kawasaki, M. & Nagaosa, N. Emergent functions of quantum materials. *Nat. Phys.* **13**, 1056–1068 (2017).
- Keimer, B., Kivelson, S. A., Norman, M. R., Uchida, S. & Zaanen, J. From quantum matter to high-temperature superconductivity in copper oxides. *Nature* **518**, 179–86 (2015).
- Hasan, M. Z. & Kane, C. L. Colloquium: topological insulators. *Rev. Mod. Phys.* **82**, 3045 (2010).
- Armitage, N. P., Mele, E. J. & Vishwanath, A. Weyl and Dirac semimetals in three-dimensional solids. *Rev. Mod. Phys.* **90**, 015001 (2018).
- Novoselov, K. S., Mishchenko, A., Carvalho, A. & Castro Neto, A. H. 2D materials and van der Waals heterostructures. *Science* **353**, aac9439 (2016).
- Zhang, J. & Averitt, R. Dynamics and control in complex transition metal oxides. *Ann. Rev. Mat. Res.* **44**, 19–43 (2014).
- Basov, D. N., Averitt, R. D. & Hsieh, D. Towards properties on demand in quantum materials. *Nat. Mater.* **16**, 1077 (2017).
- Cavalleri, A. et al. Femtosecond structural dynamics in VO<sub>2</sub> during an ultrafast solid-solid phase transition. *Phys. Rev. Lett.* **87**, 237401 (2001).
- Lee, W. S. et al. Phase fluctuations and the absence of topological defects in a photo-excited charge-ordered nickelate. *Nat. Commun.* **3**, 838 (2012).
- Trigo, M. et al. Fourier-transform inelastic x-ray scattering from time- and momentum-dependent phonon-phonon correlations. *Nat. Phys.* **9**, 790–794 (2013).
- Otto, M. R. et al. How optical excitation controls the structure and properties of vanadium dioxide. *Proc. Natl Acad. Sci. USA* **116**, 450–455 (2018).
- Sie, E. J. et al. An ultrafast symmetry switch in a Weyl semimetal. *Nature* **565**, 61–66 (2019).
- Zong, A. et al. Evidence for topological defects in a photoinduced phase transition. *Nat. Phys.* **15**, 27–31 (2019).
- Rini, M. et al. Control of the electronic phase of a manganite by mode-selective vibrational excitation. *Nature* **449**, 72–74 (2007).
- Porer, M. et al. Non-thermal separation of electronic and structural orders in a persisting charge density wave. *Nat. Mater.* **13**, 857–861 (2014).
- Coslovich, G. et al. Ultrafast dynamics of vibrational symmetry breaking in a charge-ordered nickelate. *Sci. Adv.* **3**, 1600735 (2017).
- Perfetti, L. et al. Time evolution of the electronic structure of 1T-TaS<sub>2</sub> through the insulator-metal transition. *Phys. Rev. Lett.* **97**, 067402 (2006).
- Rohwer, T. et al. Collapse of long-range charge order tracked by time-resolved photoemission at high momenta. *Nature* **471**, 490–493 (2011).
- Sobota, J. A., He, Y. & Shen, Z.-X. Electronic structure of quantum materials studied by angle-resolved photoemission spectroscopy. *Rev. Mod. Phys.* **93**, 025006 (2021).
- Sipos, B. et al. From Mott state to superconductivity in 1T-TaS<sub>2</sub>. *Nat. Mater.* **7**, 960–5 (2008).
- Cho, D. et al. Nanoscale manipulation of the Mott insulating state coupled to charge order in 1T-TaS<sub>2</sub>. *Nat. Commun.* **7**, 10453 (2016).
- Miller, D. C., Mahanti, S. D. & Duxbury, P. M. Charge density wave states in tantalum dichalcogenides. *Phys. Rev. B* **97**, 045133 (2018).
- Eichberger, M. et al. Snapshots of cooperative atomic motions in the optical suppression of charge density waves. *Nature* **468**, 799–802 (2010).
- Haupt, K. et al. Ultrafast metamorphosis of a complex charge-density wave. *Phys. Rev. Lett.* **116**, 016402 (2016).
- Vogelgesang, S. et al. Phase ordering of charge density waves traced by ultrafast low-energy electron diffraction. *Nat. Phys.* **14**, 184–190 (2017).
- Stojchevska, L. et al. Ultrafast switching to a stable hidden quantum state in an electronic crystal. *Science* **344**, 177 (2014).
- Han, T.-R. T. et al. Exploration of metastability and hidden phases in correlated electron crystals visualized by femtosecond optical doping and electron crystallography. *Sci. Adv.* **1**, e1400173 (2015).
- Luo, H. et al. Polytypism, polymorphism, and superconductivity in TaSe<sub>2-x</sub>Te<sub>x</sub>. *Proc. Natl Acad. Sci. USA* **112**, E1174–E1180 (2015).
- Sun, S. et al. Direct observation of an optically induced charge density wave transition in 1T-TaSe<sub>2</sub>. *Phys. Rev. B* **92**, 224303 (2015).
- Wei, L. et al. Dynamic diffraction effects and coherent breathing oscillations in ultrafast electron diffraction in layered 1T-TaSeTe. *Struct. Dyn.* **4**, 044012 (2017).
- Li, J. et al. Ultrafast decoupling of atomic sublattices in a charge-density-wave material. Preprint at <https://arxiv.org/abs/1903.09911> (2019).
- Wilson, J. & Yoffe, A. The transition metal dichalcogenides discussion and interpretation of the observed optical, electrical and structural properties. *Adv. Phys.* **18**, 193–335 (1969).
- Sörgel, T., Nuss, J., Wedig, U., Kremer, R. & Jansen, M. A new low temperature modification of TaTe<sub>2</sub>—comparison to the room temperature and the hypothetical 1T-TaTe<sub>2</sub> modification. *Mater. Res. Bull.* **41**, 987–1000 (2006).
- Doublet, M.-L., Remy, S. & Lemoigno, F. Density functional theory analysis of the local chemical bonds in the periodic tantalum dichalcogenides TaX<sub>2</sub> (X = S, Se, Te). *J. Chem. Phys.* **113**, 5879–5890 (2000).
- Gao, J. J. et al. Origin of the structural phase transition in single-crystal TaTe<sub>2</sub>. *Phys. Rev. B* **98**, 224104 (2018).
- Chen, C. et al. Trimer bonding states on the surface of the transition-metal dichalcogenide TaTe<sub>2</sub>. *Phys. Rev. B* **98**, 195423 (2018).
- El Baggari, I., Stiehl, G. M., Waelder, J., Ralph, D. C. & Kourkoutis, L. F. Atomic-resolution cryo-STEM imaging of a structural phase transition in TaTe<sub>2</sub>. *Microsc. Microanal.* **24**, 86–87 (2018).
- Wang, H. et al. Charge density wave and atomic trimerization in layered transition-metal dichalcogenides 1T-MX<sub>2</sub> materials. *EPL* **130**, 47001 (2020).
- Svetin, D., Vaskivskiy, I., Brazovskii, S. & Mihailovic, D. Three-dimensional resistivity and switching between correlated electronic states in 1T-TaS<sub>2</sub>. *Sci. Rep.* **7**, 46048 (2017).

40. LeBlanc, A. & Nader, A. Resistivity anisotropy and charge density wave in 2H–NbSe<sub>2</sub> and 2H–TaSe<sub>2</sub>. *Solid State Commun.* **150**, 1346–1349 (2010).
41. Chen, H., Li, Z., Guo, L. & Chen, X. Anisotropic magneto-transport and magnetic properties of low-temperature phase of TaTe<sub>2</sub>. *EPL* **117**, 27009 (2017).
42. Filippetto, D. & Qian, H. Design of a high-flux instrument for ultrafast electron diffraction and microscopy. *J. Phys. B* **49**, 104003 (2016).
43. Ji, F. et al. Ultrafast relativistic electron nanoprobes. *Commun. Phys.* **2**, 54 (2019).
44. Siddiqui, K. et al. Ultrafast structural dynamics of materials captured by relativistic electron bunches. *Proc. SPIE* **11497**, 114970J (2020).
45. Vernes, A., Ebert, H., Bensch, W., Heid, W. & Näther, C. Crystal structure, electrical properties and electronic band structure of tantalum ditelluride. *J. Condens. Matter Phys.* **10**, 761–774 (1998).
46. Erasmus, N. et al. Ultrafast dynamics of charge density waves in 4H<sub>b</sub>-TaSe<sub>2</sub> probed by femtosecond electron diffraction. *Phys. Rev. Lett.* **109**, 167402 (2012).
47. Kirkland, E. J. *Advanced Computing in Electron Microscopy* (Springer, 2010).
48. Ophus, C. A fast image simulation algorithm for scanning transmission electron microscopy. *Adv. Struct. Chem. Imaging* **3**, 13 (2017).
49. Storeck, G. et al. Structural dynamics of incommensurate charge-density waves tracked by ultrafast low-energy electron diffraction. *Struct. Dyn.* **7**, 034304 (2020).
50. Kwon, O.-H., Barwick, B., Park, H. S., Baskin, J. S. & Zewail, A. H. Nanoscale mechanical drumming visualized by 4D electron microscopy. *Nano Lett.* **8**, 3557–3562 (2008).
51. Mannebach, E. M. et al. Dynamic structural response and deformations of monolayer MoS<sub>2</sub> visualized by femtosecond electron diffraction. *Nano Lett.* **15**, 6889–6895 (2015).
52. Ubaldini, A., Jacimovic, J., Ubrigg, N. & Giannini, E. Chloride-driven chemical vapor transport method for crystal growth of transition metal dichalcogenides. *Cryst. Growth Des.* **13**, 4453–4459 (2013).
53. Castellanos-Gomez, A. et al. Deterministic transfer of two-dimensional materials by all-dry viscoelastic stamping. *2D Mater.* **1**, 011002 (2014).

## Acknowledgements

We gratefully acknowledge Nord Andresen for developing the cryogenic sample stage and other excellent engineering efforts at HiRES, Paul Ashby for performing the AFM measurement, and Germán Sciaini for stimulating discussions. K.M.S., D.F., and R.A.K. acknowledge support for the ultrafast materials UED studies by the Laboratory Directed Research and Development (LDRD) Program of Lawrence Berkeley National Lab under U.S. Department of Energy (DOE) Contract DE-AC02-05CH11231. Development and operation of the HiRES instrument (D.F. and F.C.) was supported by DOE under the same Contract No. Funding for D.B.D. was provided by STROBE: A National Science Foundation Science and Technology Center under Grant No. DMR 1548924. Work at the Molecular Foundry was supported by the DOE Office of Basic Energy Sciences under Contract No. DE-AC02-05CH11231. C.O. acknowledges support from the DOE Early Career Research Award program. A.R. gratefully acknowledges support through the Early Career LDRD Program of Lawrence Berkeley National Laboratory under DOE Contract No. DE-AC02-05CH11231. S.R. was supported through the Center for Non-Perturbative Studies of Functional Materials funded by the Computational Materials Sciences Program of the DOE Office of Basic Energy Sciences, Materials Sciences and Engineering

Division. This research used resources of the National Energy Research Scientific Computing Center, a DOE Office of Science User Facility supported by the DOE Office of Science under Contract No. DE-AC02-05CH11231. The financial support for sample preparation was provided by the National Science Foundation through the Penn State 2D Crystal Consortium-Materials Innovation Platform (2DCC-MIP) under NSF cooperative agreement DMR-1539916.

## Author contributions

K.M.S. and D.B.D. contributed equally to this work. K.M.S., D.F., and R.A.K. conceived the experiment. D.F. designed the experimental setup. K.M.S., D.B.D., F.C., and D.F. performed the UED experiments. K.M.S., D.B.D., and C.O. analysed the diffraction data and performed diffraction simulations. S.R. and L.Z.T. performed the ab initio theory calculations. Y.Z. and Z.M. synthesised TaTe<sub>2</sub> samples, and D.B.D. and J.D.C. prepared them for UED experiments. Y.Z., C.S., J.D.C., D.B.D., and A.R. characterised the sample. D.F., A.M., P.M., and R.A.K. supervised the project. All authors contributed towards data interpretations, discussions, and the manuscript.

## Competing interests

The authors declare no competing interests.

## Additional information

**Supplementary information** The online version contains supplementary material available at <https://doi.org/10.1038/s42005-021-00650-z>.

**Correspondence** and requests for materials should be addressed to D.F. or R.A.K.

**Peer review information** *Communications Physics* thanks the anonymous reviewers for their contribution to the peer review of this work.

**Reprints and permission information** is available at <http://www.nature.com/reprints>

**Publisher's note** Springer Nature remains neutral with regard to jurisdictional claims in published maps and institutional affiliations.



**Open Access** This article is licensed under a Creative Commons Attribution 4.0 International License, which permits use, sharing, adaptation, distribution and reproduction in any medium or format, as long as you give appropriate credit to the original author(s) and the source, provide a link to the Creative Commons license, and indicate if changes were made. The images or other third party material in this article are included in the article's Creative Commons license, unless indicated otherwise in a credit line to the material. If material is not included in the article's Creative Commons license and your intended use is not permitted by statutory regulation or exceeds the permitted use, you will need to obtain permission directly from the copyright holder. To view a copy of this license, visit <http://creativecommons.org/licenses/by/4.0/>.

This is a U.S. Government work and not under copyright protection in the US; foreign copyright protection may apply 2021